

High resolution multimodal clinical ophthalmic imaging system

Mircea Mujat*, R. Daniel Ferguson, Ankit H. Patel, Nicusor Iftimia, Niyom Lue, and Daniel X. Hammer

Physical Sciences Inc., 20 New England Business Center, Andover MA 01810, USA
*mujat@psicorp.com

Abstract: We developed a multimodal adaptive optics (AO) retinal imager which is the first to combine high performance AO-corrected scanning laser ophthalmoscopy (SLO) and swept source Fourier domain optical coherence tomography (SSOCT) imaging modes in a single compact clinical prototype platform. Such systems are becoming ever more essential to vision research and are expected to prove their clinical value for diagnosis of retinal diseases, including glaucoma, diabetic retinopathy (DR), age-related macular degeneration (AMD), and retinitis pigmentosa. The SSOCT channel operates at a wavelength of 1 μm for increased penetration and visualization of the choriocapillaris and choroid, sites of major disease activity for DR and wet AMD. This AO system is designed for use in clinical populations; a dual deformable mirror (DM) configuration allows simultaneous low- and high-order aberration correction over a large range of refractions and ocular media quality. The system also includes a wide field (33 deg.) line scanning ophthalmoscope (LSO) for initial screening, target identification, and global orientation, an integrated retinal tracker (RT) to stabilize the SLO, OCT, and LSO imaging fields in the presence of lateral eye motion, and a high-resolution LCD-based fixation target for presentation of visual cues. The system was tested in human subjects without retinal disease for performance optimization and validation. We were able to resolve and quantify cone photoreceptors across the macula to within ~ 0.5 deg (~ 100 - 150 μm) of the fovea, image and delineate ten retinal layers, and penetrate to resolve features deep into the choroid. The prototype presented here is the first of a new class of powerful flexible imaging platforms that will provide clinicians and researchers with high-resolution, high performance adaptive optics imaging to help guide therapies, develop new drugs, and improve patient outcomes.

©2010 Optical Society of America

OCIS codes: (110.1080) Adaptive optics, 170.4500 Optical coherence tomography, (170.0110) Imaging systems, (170.5755) Retina scanning, (170.4470) Ophthalmology

References and links

1. D. Huang, E. A. Swanson, C. P. Lin, J. S. Schuman, W. G. Stinson, W. Chang, M. R. Hee, T. Flotte, K. Gregory, C. A. Puliafito, and J. G. Fujimoto, "Optical coherence tomography," *Science* **254**(5035), 1178–1181 (1991).
2. J. Z. Liang, D. R. Williams, and D. T. Miller, "Supernormal vision and high-resolution retinal imaging through adaptive optics," *J. Opt. Soc. Am. A* **14**(11), 2884–2892 (1997).
3. A. Roorda, F. Romero-Borja, W. Donnelly III, H. Queener, T. J. Hebert, and M. C. W. Campbell, "Adaptive optics scanning laser ophthalmoscopy," *Opt. Express* **10**(9), 405–412 (2002), <http://www.opticsinfobase.org/oe/abstract.cfm?URI=oe-10-9-405>.
4. R. J. Zawadzki, S. M. Jones, S. S. Olivier, M. T. Zhao, B. A. Bower, J. A. Izatt, S. Choi, S. Laut, and J. S. Werner, "Adaptive-optics optical coherence tomography for high-resolution and high-speed 3D retinal in vivo imaging," *Opt. Express* **13**(21), 8532–8546 (2005), <http://www.opticsinfobase.org/oe/abstract.cfm?URI=oe-13-21-8532>.
5. Y. Zhang, B. Cense, J. Rha, R. S. Jonnal, W. Gao, R. J. Zawadzki, J. S. Werner, S. Jones, S. Olivier, and D. T. Miller, "High-speed volumetric imaging of cone photoreceptors with adaptive optics spectral-domain optical

- coherence tomography,” *Opt. Express* **14**(10), 4380–4394 (2006), <http://www.opticsinfobase.org/oe/abstract.cfm?URI=oe-14-10-4380>.
6. C. E. Bigelow, N. V. Iftimia, R. D. Ferguson, T. E. Ustun, B. Bloom, and D. X. Hammer, “Compact multimodal adaptive-optics spectral-domain optical coherence tomography instrument for retinal imaging,” *J. Opt. Soc. Am. A* **24**(5), 1327–1336 (2007).
 7. A. Roorda, and D. R. Williams, “The arrangement of the three cone classes in the living human eye,” *Nature* **397**(6719), 520–522 (1999).
 8. J. Carroll, M. Neitz, H. Hofer, J. Neitz, and D. R. Williams, “Functional photoreceptor loss revealed with adaptive optics: an alternate cause of color blindness,” *Proc. Natl. Acad. Sci. U.S.A.* **101**(22), 8461–8466 (2004).
 9. J. I. Wolfing, M. Chung, J. Carroll, A. Roorda, and D. R. Williams, “High-resolution retinal imaging of cone-rod dystrophy,” *Ophthalmology* **113**(6), 1014–1019 (2006).
 10. D. C. Gray, R. Wolfe, B. P. Gee, D. Scoles, Y. Geng, B. D. Masella, A. Dubra, S. Luque, D. R. Williams, and W. H. Merigan, “In vivo imaging of the fine structure of rhodamine-labeled macaque retinal ganglion cells,” *Invest. Ophthalmol. Vis. Sci.* **49**(1), 467–473 (2008).
 11. K. Kurokawa, S. Makita, and Y. Yasuno, “1 μ m wavelength adaptive optics scanning laser ophthalmoscope”, in *Ophthalmic Technologies XIX*, F. Manns, P.G. Soderberg, and A. Ho, eds., *Proc. SPIE* **7163**, 71630I, 2009.
 12. K. Kurokawa, K. Sasaki, S. Makita, M. Yamanari, B. Cense, and Y. Yasuno, “Simultaneous high-resolution retinal imaging and high-penetration choroidal imaging by one-micrometer adaptive optics optical coherence tomography,” *Opt. Express* **18**(8), 8515–8527 (2010), <http://www.opticsinfobase.org/oe/abstract.cfm?URI=oe-18-8-8515>.
 13. B. Povazay, K. Bizheva, B. Hermann, A. Unterhuber, H. Sattmann, A. F. Fercher, W. Drexler, C. Schubert, P. K. Ahnelt, M. Mei, R. Holzwarth, W. J. Wadsworth, J. C. Knight, and P. S. Russell, “Enhanced visualization of choroidal vessels using ultrahigh resolution ophthalmic OCT at 1050 nm,” *Opt. Express* **11**(17), 1980–1986 (2003), <http://www.opticsinfobase.org/oe/abstract.cfm?URI=oe-11-17-1980>.
 14. A. Unterhuber, B. Povazay, B. Hermann, H. Sattmann, A. Chavez-Pirson, and W. Drexler, “In vivo retinal optical coherence tomography at 1040 nm - enhanced penetration into the choroid,” *Opt. Express* **13**(9), 3252–3258 (2005), <http://www.opticsinfobase.org/oe/abstract.cfm?URI=oe-13-9-3252>.
 15. R. Huber, D. C. Adler, V. J. Srinivasan, and J. G. Fujimoto, “Fourier domain mode locking at 1050 nm for ultra-high-speed optical coherence tomography of the human retina at 236,000 axial scans per second,” *Opt. Lett.* **32**(14), 2049–2051 (2007).
 16. B. Povazay, B. Hermann, A. Unterhuber, B. Hofer, H. Sattmann, F. Zeiler, J. E. Morgan, C. Falkner-Radler, C. Glittenberg, S. Blinder, and W. Drexler, “Three-dimensional optical coherence tomography at 1050 nm versus 800 nm in retinal pathologies: enhanced performance and choroidal penetration in cataract patients,” *J. Biomed. Opt.* **12**(4), 041211 (2007).
 17. M.K. Yoon, A. Roorda, Y. Zhang, C. Nakanishi, L.-J.C. Wong, Q. Zhang, L. Gillum, A. Green, and J.L. Duncan, “Adaptive Optics Scanning Laser Ophthalmoscopy Images Demonstrate Abnormal Cone Structure in a Family with the Mitochondrial DNA T8993C Mutation,” *Invest. Ophthalmol. Vis. Sci.* **08–2029** (2008).
 18. C. Torti, B. Povazay, B. Hofer, A. Unterhuber, J. Carroll, P. K. Ahnelt, and W. Drexler, “Adaptive optics optical coherence tomography at 120,000 depth scans/s for non-invasive cellular phenotyping of the living human retina,” *Opt. Express* **17**(22), 19382–19400 (2009), <http://www.opticsinfobase.org/oe/abstract.cfm?URI=oe-17-22-19382>.
 19. J. R. Zawadzki, M. S. Jones, D. Chen, S. S. Choi, W. J. Evans, S. S. Olivier, and S. J. Werner, “Combined adaptive optics: optical coherence tomography and adaptive optics: scanning laser ophthalmoscopy system for retinal imaging”, in *Ophthalmic Technologies XIX*, F. Manns, P. Soderberg, and A. Ho, eds., *Proc. SPIE* **7163**, 71630F, 2009.
 20. R. D. Ferguson, Z. Zhong, D. X. Hammer, M. Mujat, A. H. Patel, Z. Deng, W. Zou, and S. A. Burns, “Adaptive optics SLO with integrated wide-field retinal imaging and tracking,” submitted to *JOSA* (2010).
 21. D. X. Hammer, M. Mujat, N. Iftimia, N. Lue, and D. Ferguson, “Multimodal Adaptive Optics for Depth Enhanced High Resolution Ophthalmic Imaging”, in *Ophthalmic Technologies XX*, F. Manns, P.G. Söderberg, and A. Ho, eds., *Proc. SPIE* **7163**, 71630J, 2010.
 22. T. E. Ustun, N. V. Iftimia, R. D. Ferguson, and D. X. Hammer, “Real-time processing for Fourier domain optical coherence tomography using a field programmable gate array,” *Rev. Sci. Instrum.* **79**(11), 114301 (2008).
 23. A.N.S.I. (ANSI), *American National Standard for the Safe Use of Lasers*. 2000, American National Standard Institute, Inc.
 24. F. C. Delori, R. H. Webb, and D. H. Sliney, “Maximum Permissible Exposures for Ocular Safety (ANSI 2000), with Emphasis on Ophthalmic Devices,” *J. Opt. Soc. Am. A* **24**(5), 1250–1265 (2007).
 25. D. C. Chen, S. M. Jones, D. A. Silva, and S. S. Olivier, “High-resolution adaptive optics scanning laser ophthalmoscope with dual deformable mirrors,” *J. Opt. Soc. Am. A* **24**(5), 1305–1312 (2007).
 26. Y. L. Chen, D. M. de Bruin, C. Kerbage, and J. F. de Boer, “Spectrally balanced detection for optical frequency domain imaging,” *Opt. Express* **15**(25), 16390–16399 (2007), <http://www.opticsinfobase.org/oe/abstract.cfm?URI=oe-15-25-16390>.
 27. D. X. Hammer, R. D. Ferguson, J. C. Magill, M. A. White, A. E. Elsner, and R. H. Webb, “Image stabilization for scanning laser ophthalmoscopy,” *Opt. Express* **10**(26), 1542–1549 (2002), <http://www.opticsinfobase.org/oe/abstract.cfm?URI=oe-10-26-1542>.

28. D. X. Hammer, R. D. Ferguson, J. C. Magill, M. A. White, A. E. Elsner, and R. H. Webb, "Compact scanning laser ophthalmoscope with high-speed retinal tracker," *Appl. Opt.* **42**(22), 4621–4632 (2003).
29. D. X. Hammer, R. D. Ferguson, T. E. Ustun, C. E. Bigelow, N. V. Iftimia, and R. H. Webb, "Line-scanning laser ophthalmoscope," *J. Biomed. Opt.* **11**(4), 041126 (2006).
30. D. X. Hammer, R. D. Ferguson, C. E. Bigelow, N. V. Iftimia, T. E. Ustun, and S. A. Burns, "Adaptive optics scanning laser ophthalmoscope for stabilized retinal imaging," *Opt. Express* **14**(8), 3354–3367 (2006), <http://www.opticsinfobase.org/oe/abstract.cfm?URI=oe-14-8-3354>.
31. W. Zou, X. Qi, and S. A. Burns, "Wavefront-aberration sorting and correction for a dual-deformable-mirror adaptive-optics system," *Opt. Lett.* **33**(22), 2602–2604 (2008).
32. D. Lowe, "Method and apparatus for identifying scale invariant features in an image and use of same for locating an object in an image," US Patent number: 6,711,293 (2004).
33. M. Mujat, R. D. Ferguson, N. Iftimia, and D. X. Hammer, "Compact adaptive optics line scanning ophthalmoscope," *Opt. Express* **17**(12), 10242–10258 (2009), <http://www.opticsinfobase.org/oe/abstract.cfm?URI=oe-17-12-10242>.
34. P. J. Burt, and E. H. Adelson, "A Multiresolution Spline with Application to Image Mosaics," *ACM Trans. Graph.* **2**(4), 217–236 (1983).
35. C. A. Curcio, and K. R. Sloan, "Packing geometry of human cone photoreceptors: variation with eccentricity and evidence for local anisotropy," *Vis. Neurosci.* **9**(2), 169–180 (1992).
36. M. Pircher, B. Baumann, E. Götzinger, and C. K. Hitzenberger, "Retinal cone mosaic imaged with transverse scanning optical coherence tomography," *Opt. Lett.* **31**(12), 1821–1823 (2006).
37. B. Potsaid, J. Liu, Y. Chen, I. Gorczynska, V. J. Srinivasan, S. Barry, J. Jiang, A. Cable, V. Manjunath, J. S. Duker, and G. J. Fujimoto, "Ultrahigh speed volumetric OCT ophthalmic imaging at 800nm and 1050nm", in *Ophthalmic Technologies XX*, F. Manns, P.G. Soderberg, and A. Ho, eds., *Proc. SPIE* **7163**, 2010.
38. T. Y. P. Chui, H. X. Song, and S. A. Burns, "Adaptive-optics imaging of human cone photoreceptor distribution," *J. Opt. Soc. Am. A* **25**(12), 3021–3029 (2008).

1. Introduction

Scanning laser ophthalmoscopy (SLO) and optical coherence tomography (OCT) provide information on cellular and sub-cellular structures in the living eye when enhanced with adaptive optics (AO) capabilities. OCT uses low-coherence interferometry to de-couple axial resolution from the diffraction-limited depth-of-focus for high resolution optical depth sectioning [1]. AO enhances transverse resolution and confocal sectioning capabilities by detecting and correcting ocular aberrations in real-time. AO has been integrated into instruments for full-field fundus imaging [2], SLO [3], and Fourier domain (FD) OCT [4–6].

AO has also become a valuable tool for vision researchers to explore the structural and functional aspects of vision and its disruption by disease [2,7–11]. While AO has yet to fully transition from research lab to clinic, OCT is now a standard diagnostic procedure for glaucoma, macular holes, macula edema, retinal detachments, and other retinal pathologies. FDOCT has now supplanted time-domain OCT for most applications because of its well-known advantages of higher speeds, higher signal-to-noise ratio (SNR), and lower phase noise. Clinical FDOCT systems are available commercially from several companies.

FDOCT comes in two basic varieties: either a rapidly tuned or swept light source is used in the source arm of the interferometer (SS), or a spectrometer is used in the detection arm (SD). In FDOCT one has to detect spectral interference fringes as function of the wave number and this can be done either sequential in time as the wavelength is swept (SS) or simultaneous with a spectrometer (SD). Each technique has advantages and disadvantages, but in general, SDOCT systems usually have slightly better axial resolution due to availability of broadband light sources (superluminescent diodes or mode-locked femtosecond lasers in the NIR) while SSOCT systems have increased depth range due to the narrower instantaneous linewidth of swept sources and very high sampling rate. SSOCT systems use discrete detectors (Si, GaAs, etc.) and are used at longer wavelengths. Ophthalmic OCT research systems at 1 μm , including initial reports configured with AO [12] have shown significantly improved choroidal penetration compared to 850 nm systems [13–17], due to reduced scattering cross-section and ocular dispersion [18].

SLO and OCT are complementary retinal imaging techniques [19]. OCT is usually cross-sectional (i.e., lateral-axial) with micron level axial resolution that yields excellent sectioning capability and is therefore better suited for visualization of retinal layers. SLO is a confocal

dimensions of each component. All imaging scanners and DMs are placed at pupil conjugates to pivot about and/or correct at a common pupil plane. The tracking galvanometers are placed at conjugates to the eye's center-of-rotation to simultaneously track retinal and pupil shifts.

The 1 μm swept source for OCT imaging (Santec Corporation, Aichi, Japan) has an average output power of 11 mW, a bandwidth (BW) of 79 nm centered at ~ 1070 nm, and a duty cycle of 0.65. This bandwidth provides a theoretical axial resolution of 4.6 μm in tissue. All other illumination sources are superluminescent diodes (SLD) that reduce image speckle and tracker noise. The SLO illumination beam centered at ~ 750 nm (14 nm BW) also acts as the wavefront sensor beacon. The LSO illumination beam is centered at 830 nm (26 nm BW) and the tracker beam is centered at ~ 915 nm. All sources are combined with off-the-shelf dichroic beamsplitters except for one, which was custom made to reflect both the 1 μm OCT and 750 nm SLO NIR beams while transmitting the 830 nm LSO and 915 nm RT beams. The power of the LSO beam at the cornea was <500 μW , far smaller than the ANSI limits for this wavelength (830 nm) and field size (33 deg line scan). The SLO power was <500 μW and the OCT power at the cornea was <2.6 mW. The combined power in all beams was below the ANSI laser safety thresholds for continuous exposure in the current imaging configuration [23,24].

The design includes a dual mirror (i.e., woofer-tweeter) AO approach for optimal aberration compensation [25]. The Hartmann-Shack wavefront sensor (HS-WS) uses a lenslet array (Adaptive Optics Associates, Cambridge, MA) and a CCD camera (Uniq Vision Inc. Santa Clara, CA) to sample the wavefront across the pupil. A lens relay and iris are used in front of the HS-WS to reduce reflection artifact from the cornea. The SLO channel uses a confocal pinhole and avalanche photodiode (APD, Hamamatsu Inc., Japan) to collect light returning from the retina. The OCT channel is configured in a customary swept source-based architecture (a.k.a. optical Fourier domain interferometry) and uses a circulator, 2×2 fiber coupler, and balanced detector approach [26] for efficient light collection and common mode signal rejection. The optical delay line uses a folded arrangement - five passes off a pair of mirrors - to match the ~ 4.3 m sample pathlength.

The RT hardware is fully integrated into the AO beam path to provide optimal tracking performance [20]. The active retinal tracker operates by directing a separate beam onto a retinal target (usually the bright lamina cribrosa in the ONH) and sensing phase shifts when the eye moves [27,28]. The resultant error signals are fed back in high speed closed loop fashion into two transverse galvanometers to maintain lock. In addition to the new integrated design for AO applications, the retinal tracker instrumentation configuration includes an FPGA-based tracking control board, which performs digital lock-in amplification and other signal processing for robust operation. The tracking system maintains lock with an accuracy <10 μm [24] based on closed loop control.

The line scanning ophthalmoscope (LSO) provides a wide field (~ 33 deg) confocal view of the retina for scan placement and initial target identification [29]. The OCT/SLO scan engine is configured to use a resonant scanner (RS) and single galvanometer for SLO imaging and two galvanometers for OCT imaging. The OCT scan (line, circle, raster, radial, etc.) can be translated and centered anywhere in the wide field of the AO beam path by adjusting offset voltages to the galvanometers. Similarly, the SLO flying spot raster scan can be centered and shifted anywhere in the AO beam path for acquisition of montages and strips. However, because the SLO RS cannot be driven with voltage offsets, the x-axis OCT galvanometer serves the dual function of shifting the SLO raster in this mode.

The Zemax optical model of the primary beam path with a 6 deg off-axis scan is shown in Fig. 2. The predominant system aberrations are defocus and astigmatism, which are easily corrected with either mirror, the woofer (Mirao, Imagine Eyes, Orsay, France) or the tweeter (Boston Micromachines Corporation, Cambridge, MA), but better corrected with the former because the larger amplitude of low-order aberrations require a smaller fraction of the mirror total range. The system RMS error, shown in Fig. 2(b) is 0.64λ (0.48 μm). The Mirao DM

requires a total surface stroke of $\sim 1.5 \mu\text{m}$ to correct the system aberrations. The RMS error after simulated AO correction [Fig. 2(c)] is 0.005λ ($0.00375 \mu\text{m}$). The maximum stroke needed over the entire 33 deg field for system aberration is $< 4 \mu\text{m}$.

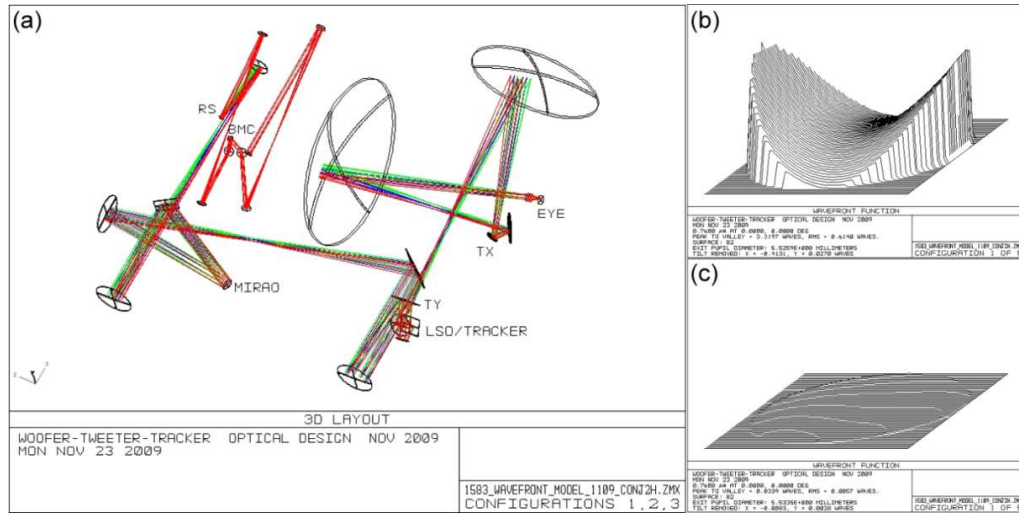


Fig. 2. Optical performance modeled in Zemax. (a) Optical layout with 6 deg. off-axis scan (from the pole of the paraxial eye). Wavefront function map (b) without and (c) with AO compensation.

2.2 Instrumentation

The system instrumentation includes three framegrabbers (one dual camera), two cameras, two detectors, four sources, five galvanometers, three resonant scanners, a motorized stage, two deformable mirror controllers, and five custom electronics boards designed and fabricated by PSI. All system instrumentation is contained in two electronics boxes and housed in a small instrumentation rack for portability. The tracker box currently contains only the LSO source and all the system galvanometers; a future upgrade will include the RT source, the tracking RS pair and a custom electronic board to control the retinal tracker in a high bandwidth closed loop manner.

The imaging box contains three custom electronics boards: the real-time OCT digitizer, the FDOCT processing board [22], and the SLO timing board. It also contains the SLO sources, the voltage-controlled RS driver board, and the OCT delay line stage controller. The RS amplitude (which sets the SLO size) is controlled via the host computer with an analog waveform output from the SLO timing board. Because the OCT swept source (20 kHz sweep rate) and the SLO RS (14.5 kHz scan rate) are not synchronized, SLO and OCT imaging are performed in rapid sequence rather than simultaneously. To provide seamless switching between OCT and SLO modes using the same scanning and processing hardware, a switch directs either the RS or swept source sync signals to the high speed digitizer. Both are TTL signals in the kHz range. The digitizer generates a pixel clock (50 MHz), duplicates the line sync, and generates a frame sync signal, which are all passed to the framegrabbers via the real time OCT processing board. The real time processing board generates all the waveforms to drive the galvanometers. Thus the HS-WS camera (and hence the correction) is always synchronized to the primary imaging hardware. This prevents a drift in the AO correction across the imaging field. It is not necessary to synchronize the LSO scan. In OCT mode, the signal from the balanced detector generated from the fiber interferometer is input to the high speed digitizer. This signal is not used in SLO mode. Communication between the digitizer, real time OCT processing board, and framegrabbers is accomplished with the CameraLink interface. The resonant scanner is turned off for AO-OCT operation. Because we have

configured the instrumentation so that a single switch can change modes, it only takes a few seconds to change from SLO to OCT imaging and vice versa. The software is flexible allowing for images to be sequentially acquired at the same eccentricity or full sets of data can be acquired with each modality independently. Both light sources are left on because the SLO source acts as the AO beacon. The OCT source can be turned off during SLO imaging but since the combined power is less than the ANSI threshold, it is not necessary to do this.

The SLO timing board (Fig. 3) has a novel FPGA-based design to provide further device automation and enhanced performance (e.g., increase SNR from a stable blanking region). The functionality of the timing board includes: generation of a non-linear pixel clock (PCLK) for automatic SLO image dewarping; automatic electronic video blanking via high speed analog signal multiplexing; generation of SLO/OCT waveforms and offsets (under user control); generation of the SLO RS amplitude control signal (under user control); and dual channel video operation for simultaneous reflectance/fluorescence imaging.

2.3 Human subjects and imaging procedure

The multimodal AO retinal imager was tested in six subjects to demonstrate performance capabilities. The subjects were aged between 23 and 53 years and the refractive error was between 0 and 7D (all myopes). A human subject protocol was approved by New England IRB prior to imaging and all subjects gave informed consent to be imaged. Some of the subjects with small pupils were dilated to enhance AO correction. Subjects that were not dilated often had larger variability in AO and imaging performance, especially when imaging the fovea, which generally caused the pupil to constrict (from the 760-nm SLO beam). All subjects used a bite bar for head stabilization and pupil centration.

The imaging sessions did not follow a set protocol but included OCT cross-sectional and raster scans (1-3 mm), SLO images (1 and 2 deg fields), strip scans, and montages. The montage scans step the SLO offset galvanometers over a matrix with overlap, the size of which (2×2 , 3×3 , 4×4 , etc.) is configured by the user [30]. The SLO strip scanning is an innovation whereby the SLO offset galvanometers are slowly scanned in the horizontal or vertical direction to pan across a retinal patch and produce a stack of images that are significantly overlapping. This aids in automated registration, especially in the presence of excessive eye motion.

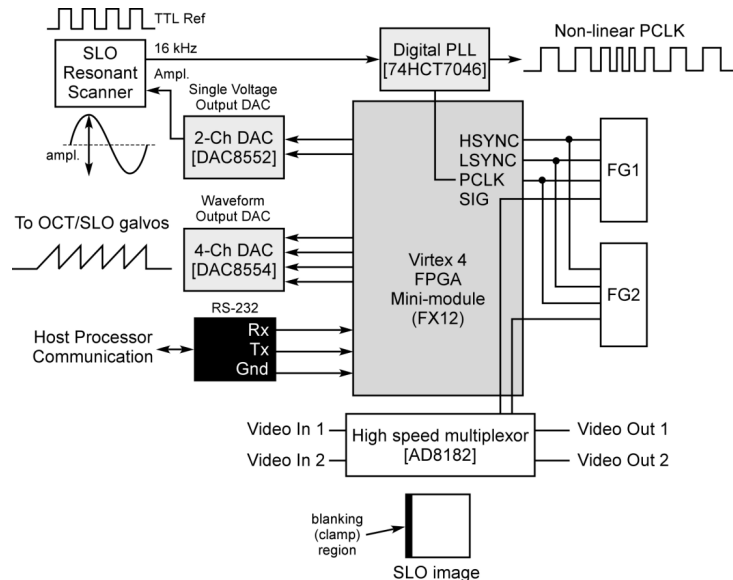


Fig. 3. SLO timing board diagram.

3. Results

3.1 AO performance

The system optical performance was characterized first using diffusely reflecting targets at various retinal (i.e., focal) conjugates and compared to the Zemax optical model presented above. Next, the system and AO performance were tested using a model eye consisting of a 25 mm focal length achromat and a diffusely reflecting “retina” (business card paper). Finally, the AO correction performance was measured in live human eyes.

In initial human subject testing of the dual-DM approach, a simplified control algorithm was used whereby the woofer corrected system and lower-order sample aberrations and the tweeter corrected sample higher-order aberrations. In order to prevent the dual-DM control from causing the correction to oscillate (especially since the response time differed between mirrors), the woofer was initiated first and run in static mode where it would correct the wavefront for a fixed number of cycles and then held while the tweeter was activated and left in dynamic mode. The minimum number of static cycles was chosen to insure proper lower-order aberration correction. At the retinal conjugates and in the model eye, both DMs were used although the tweeter corrected only a very small amount of residual aberration. We are currently implementing a dual-DM control algorithm, based upon the one described by Zou et al. [31], that will provide better stability AO correction.

The validation at retinal conjugates and in the model eye was performed by direct measurement of the point spread function (PSF) independent of the HS-WS at a plane conjugate to the SLO detector pinhole using a standard USB CCD camera. The magnification from the SLO confocal pinhole (and CCD position) to the retina is ~ 9.25 so a $100\ \mu\text{m}$ pinhole projects to roughly $11\ \mu\text{m}$ on the retina, or ~ 2.2 times the $4.9\ \mu\text{m}$ Airy disc at $750\ \text{nm}$. A $200\ \mu\text{m}$ pinhole ($\sim 22\ \mu\text{m}$ on the retina) is less confocal allowing more scattered and aberrated light without improving imaging, while a $50\ \mu\text{m}$ pinhole ($5.4\ \mu\text{m}$ on the retina) is tightly confocal: only 1.1 times the Airy disc. In general, we imaged first with the $100\ \mu\text{m}$ pinhole, and used the $50\ \mu\text{m}$ pinhole for increased contrast in subjects with bright macula, or used the $200\ \mu\text{m}$ pinhole for undilated subjects and subjects with dim macula. Larger pinholes were also used to image vessels.

The PSF at two retinal conjugates (one between the DMs and another on the front end) for focused illumination are shown in the first three columns in Fig. 4. Note that the system aberration is minimal at the second conjugate (in front of the DMs) with some residual astigmatism. The PSF FWHM (full width half maximum, average of x and y) is $88\ \mu\text{m}$ ($9.5\ \mu\text{m}$ at retina). At the retinal conjugate between the DMs however, there are significantly more lower order aberrations - the PSF FWHM nearly doubles to $\sim 152\ \mu\text{m}$ without AO correction. With AO correction, the PSF FWHM is $83\ \mu\text{m}$, less than two times the Airy disc size.

Figure 4 also shows the PSF in a model eye with and without AO correction (columns 4-5). With AO correction (both DMs activated), the FWHM decreases to ~ 127 from $243\ \mu\text{m}$. (The CCD may have been slightly saturated, causing a slight overestimation of the PSF width). Some residual astigmatism remains, but AO significantly improves the PSF approximately to the size of the confocal pinhole. In the model eye, AO correction reduced the RMS error from $\sim 0.6\ \mu\text{m}$ to $< 0.05\ \mu\text{m}$ and increased the Strehl ratio to 0.92 (as measured by the wave aberration function from the HS-WS).

An example of the AO performance achieved in one human subject is shown in Fig. 5. Illustrated are the wavefront error map (top row) and the PSF (second row) for three cases: no AO correction (first column), DM1 (woofer) correction (second column), and dual-DM (woofer-tweeter) correction (third column). The time course of the correction and the aberrations separated by Zernike order are also shown. The average RMS wavefront error (Strehl ratio) for the three cases was 1.215 (< 0.01), 0.097 (0.52), and 0.052 (0.83) μm , respectively. Thus, the dual-DM approach achieved more optimal AO correction (diffraction limited) in human subjects than could be achieved with a single mirror alone.

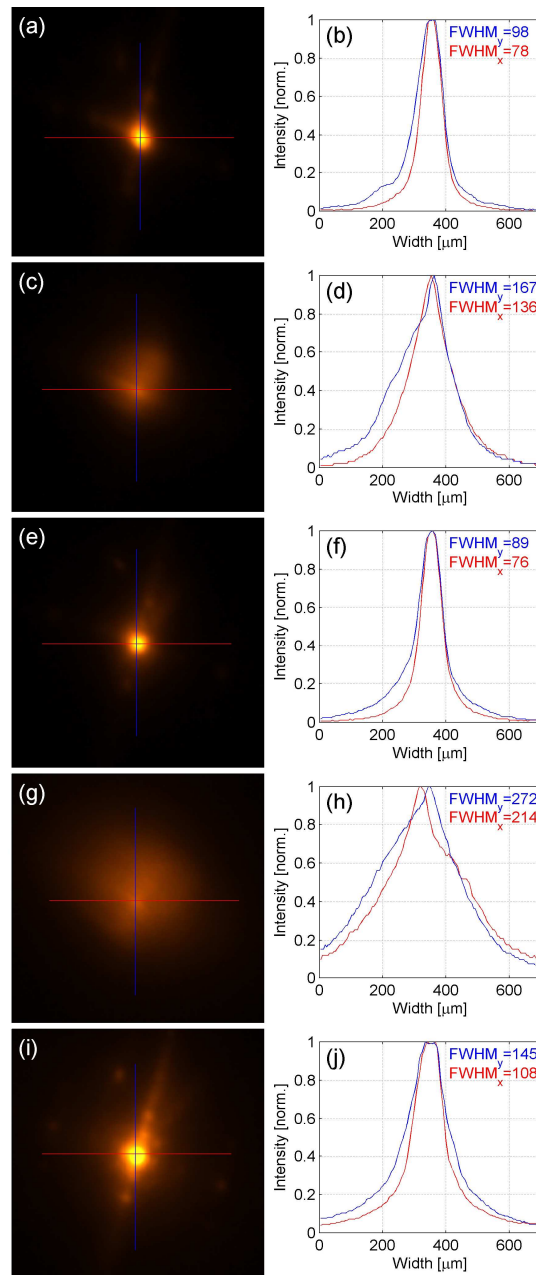


Fig. 4. AO performance in artificial targets. Shown are the measured PSF (left column) from light focused on diffuse target and horizontal and vertical line profiles (right column). Measurements were made: (a),(b) at a retinal conjugate in between the DMs; (c),(d) at a second retinal conjugate in front of the DMs (towards the eye) without AO correction; (e),(f) at the second retinal conjugate with AO correction; (g),(h) in a model eye without AO correction; and (i),(j) in a model eye with AO correction. FWHM values are listed on the graphs.

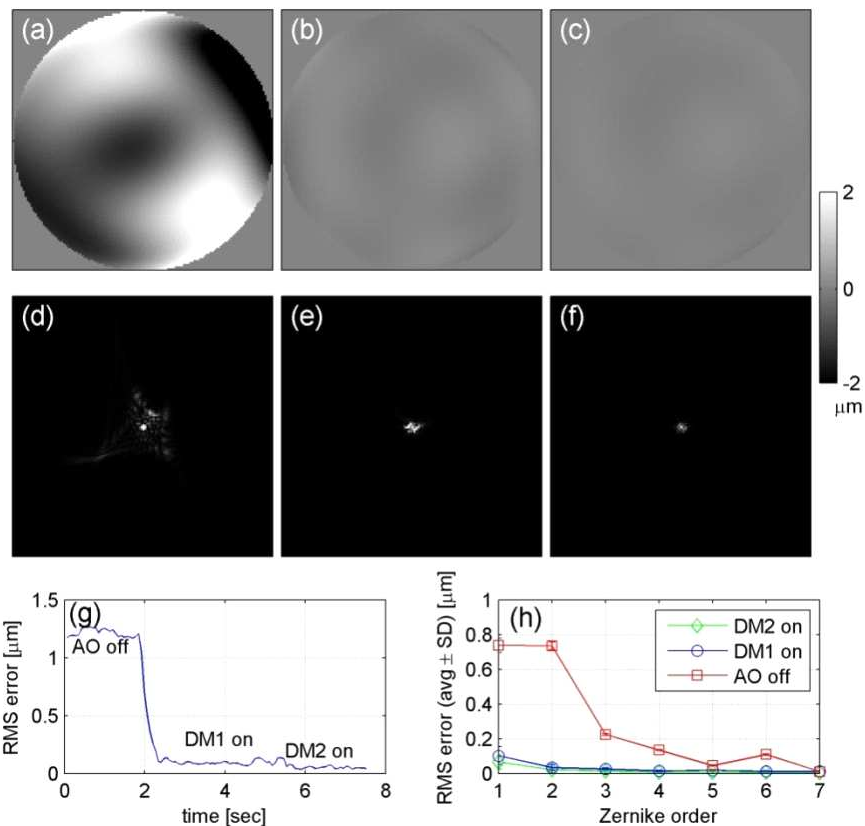


Fig. 5. AO performance in a human eye. (a)-(c) Wavefront error map and (d)-(e) point spread function for no AO correction, single DM, and dual DM correction. (g) Time course of AO correction. (h) RMS error by Zernike order.

3.2 Imaging performance

Examples from 4 of the 6 subjects in each of the three primary imaging modes (LSO, SLO, OCT) are shown in Fig. 6. The LSO image provides a 33 deg wide field view of the retina. The 2 deg SLO images were taken near the fovea. Cone photoreceptors can be resolved to within ~ 0.5 deg (100-150 μm) of the fovea. The cross-sectional OCT image spans 2 mm (6.9 deg) centered on the fovea. The OCT images are composites of between 5 and 10 frames after flattening and alignment. Ten major retinal layers (nerve fiber, ganglion cell, inner plexiform, inner nuclear, outer plexiform, outer nuclear, inner segments, outer segments, retinal pigment epithelium, choriocapillaris) can be resolved.

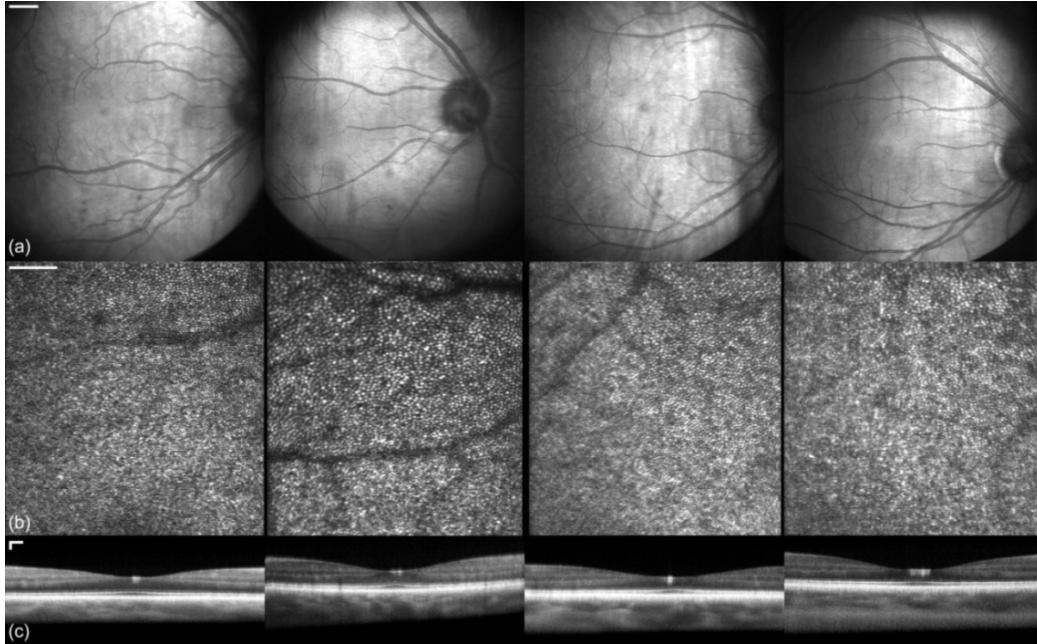


Fig. 6. LSO (a), AOSLO (b), and AO-SSOCT (c) images collected from four human subjects aged 23 to 50. SLO images are single 2 deg scans taken near the fovea (visible at the bottom of the frame). LSO and OCT images are composite images created by averaging between 5 and 10 frames. OCT and SLO scalebars are 100 μm . LSO scalebar is 1 mm.

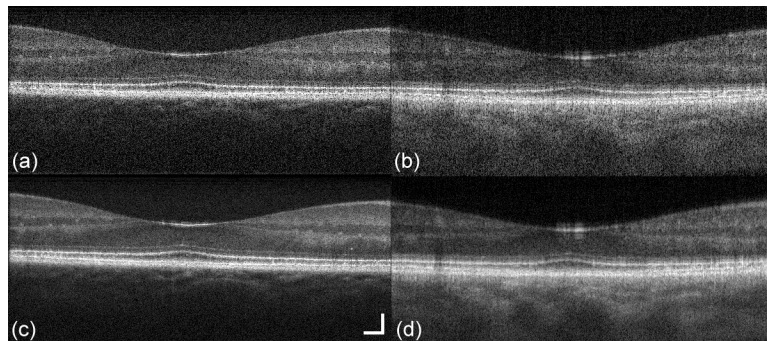


Fig. 7. Qualitative comparison of increased choroidal penetration at 1 μm wavelength. (a) and (c) are single and 4-frame composite 850 nm AO-SDOCT images. (b) and (d) are single and 4-frame composite 1 μm AO-SSOCT images. The scalebar is 100 μm .

An AOSLO montage in the central ~ 3 deg for one subject is shown in Fig. 8. The montage was created by manually stitching together a 3×3 matrix of 2 deg AOSLO images. The magnified regions to the right indicate excellent cone contrast within 0.5 deg. ($\sim 150 \mu\text{m}$) of the fovea center.

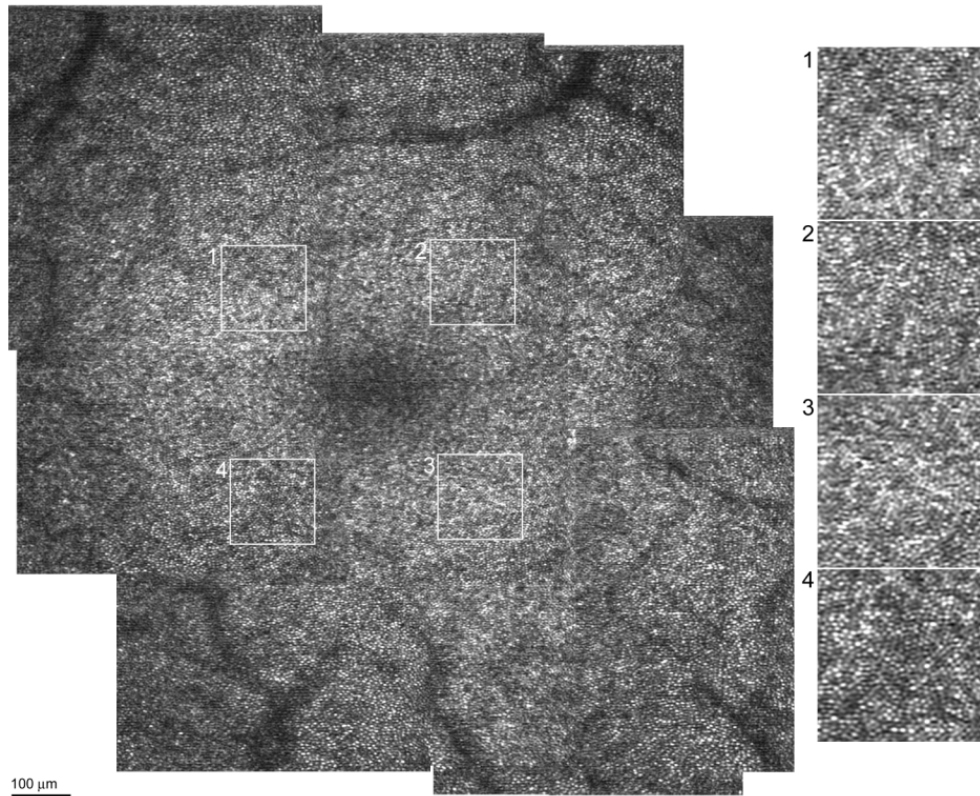


Fig. 8. AOSLO montage in the central macula ([Media 1](#), [Media 2](#)).

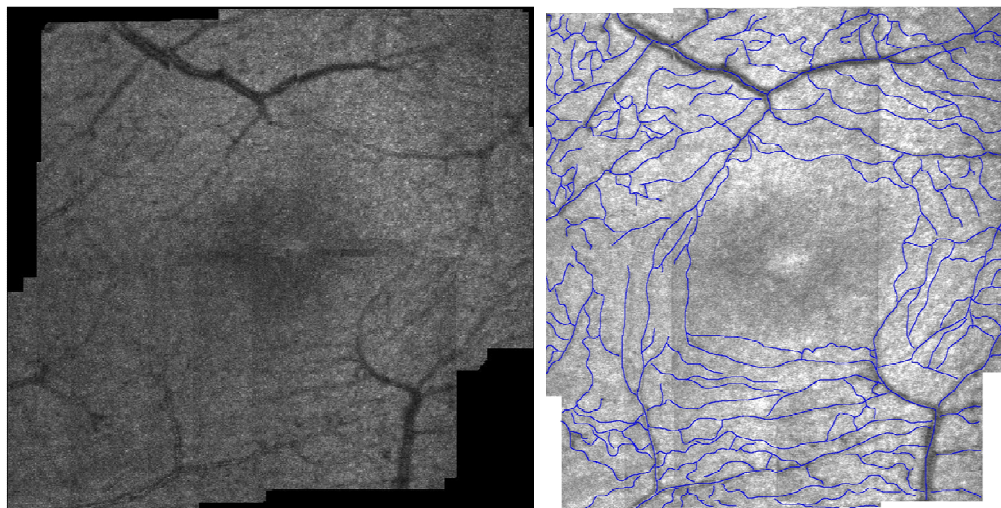


Fig. 9. Automatic montage (left). ([Media 3](#)). Manual montage (right) with manual tracing of the blood vessels to illustrate the a-vascular zone.

For generating a large area montage we employed a snake-like scan pattern resembling an S. The operator can choose the number of frames acquired at each location, the overlap percentage for pairs of sequential locations, and the size of the montage. Another option is to perform the montage using continuous slow strip scan as described above. Figures 8 and 9 show 3×3 montages of 2 deg scans with 50% overlap stitched manually (Fig. 8) or

automatically (Fig. 9). The auto-stitching algorithm is based on the scale invariant feature transform (SIFT) [32] to match and then align frames as described in detail elsewhere [33]. For auto-stitching, we used a whole frame translation approach with the average displacement from all matched points. Each new frame was stitched to the entire montage obtained to that point. Inter-frame eye motion often helps to increase overlap between frames. In the overlap region the program selects the frame that has the best contrast. Alternatively, one can use multi-frame averaging [33] or seamless patching using multi-band blending as developed by Bur and Adelson [34]. The right image in Fig. 9 shows the blood vessels manually traced to illustrate the foveal avascular zone.

Cone photoreceptor counts were performed on several retinal patches at various eccentricities from a single 2-deg. image. AOSLO scan near the fovea (identifiable in the images) for 4 subjects using manual and automated methods (Fig. 10). The automated cone photoreceptor counting algorithm corrects for a non-uniform image background, applies morphological operators, and uses a centroiding algorithm for initial identification of cone locations. The locations are then filtered to provide a final cone count in the retinal patch examined. The final filter parameter is set according to the eccentricity and requires some limited user input. The manual (solid symbols) and automated (open symbols) results are compared to previously reported histology [35] shown as a solid line. In general, the automated result showed good correspondence with the manual counts and histology. For lower eccentricities close to the resolution limit of the instrument, the algorithm begins to break down and underestimate the count.

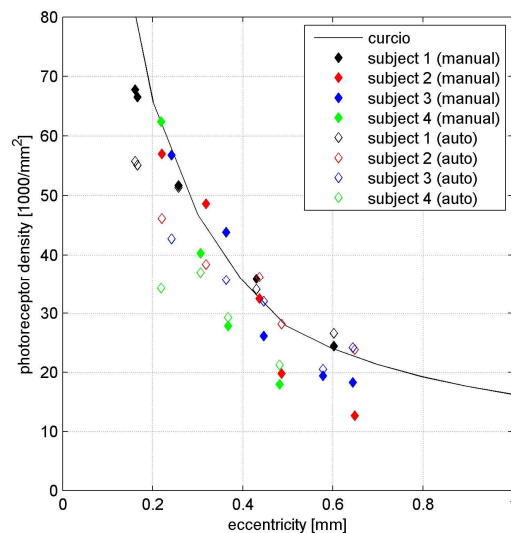


Fig. 10. Photoreceptor counting results.

4. Discussion

The multimodal AO retinal imager is a powerful platform for the investigation of retinal diseases. The capabilities of this platform include acquisition of AO-corrected SLO and OCT images, wide dynamic range AO-correction with the dual-DM approach, retinal tracking, and auxiliary wide-field LSO imaging. Future studies will fully characterize the depth enhancement with the 1 μm OCT source. In this preliminary report, we demonstrate initial AO performance, SLO imaging of the photoreceptor mosaic and OCT images.

SLO and OCT are neither equivalent nor interchangeable imaging technologies. Consider, for example, the routine ability of AOSLO to resolve photoreceptors (in some instances within $<100 \mu\text{m}$ of the fovea), which most vision researchers and clinicians would agree

constitutes a powerful capability for understanding and treating many retinal diseases. Photoreceptors are, after all, the point of optical-neural transduction and thus the starting point of the visual pathway. Recent reports of photoreceptor and RPE cell resolution with OCT [36,18,37], often without AO, may lead some to question whether the AO multimodal approach, with accompanying additional system complexity is justified. While OCT may resolve photoreceptors at some large eccentricities with en-face [36] or ultra-high speed systems [15] to partially overcome eye motion artifacts, to date only the AOSLO approach has allowed for relatively rapid mapping of the cone mosaic across large parts of the macula [38]. The correction of ocular aberrations with AO is essential for either technique to resolve fine scale structures that distinguish coherence artifacts from biological constituents. On the other hand, OCT offers unparalleled axial discrimination of disruption, thinning, or thickening of the retinal layers that are often the first signs of pathology even before changes in ophthalmoscopic appearance. Therefore, correlative multimodal AO systems may be the best approach to examination of disease attributes. We are currently developing automated image acquisition and analysis techniques to address the difficulties that arise from system complexity.

One major advantage of AO-OCT is improved lateral resolution that would allow imaging the 3-D spatial structure of the photoreceptor layers. The 2-D local spatial patterns of cones, etc., are readily seen in small AOSLO image fields. However, small OCT B-scans of 1-2 deg, traversing the cone mosaic along one line, even at high resolution are harder to interpret; it is not necessarily a simple matter to prove that such structure is not speckle. The best way to do this is to produce a 3-D volumetric image and segment out the relevant layers which reveal the mosaic. Unfortunately, in the present system, the swept-source employed, in addition to having considerable intensity noise, is limited to 20 kHz A-line rate. The resulting 3-D frame rate is too slow to capture a local mosaic, due principally to eye motion. Eye tracking can help significantly, but initial tests have shown that stabilization must be to less than one cone diameter (typically $<5\ \mu\text{m}$, to avoid disrupting the pattern beyond recognition) and no tracking methods yet available have that kind of precision. Transversal scanning SLO/OCT methods have shown somewhat better performance, at the price of returning to the time domain and using axial tracking [36]. High speed SDOCT methods (Basler Sprint, 140 kA-lines/s) have proven much more effective, but met with limited success. At 1070 nm, new MEMS swept-sources (Exalos, Axsun) or the FDML [37] approaches are likely to attain the requisite speed to achieve the full promise of AO SLO/OCT. The important thing to recognize however, is that all of these OCT technologies are amenable to improvement, while the focus of this study was the AO-based multimodal clinical imaging.

While the most desirable clinical scenario is to enable acquisition of all imaging modes simultaneously, one disadvantage of our current approach (i.e., OCT channel using a swept source) is caused by the necessity of acquiring the SLO image at the RS frequency (14.16 kHz) and the OCT image at the swept source frequency (20 kHz). We have therefore configured the multimodal AO system to sequentially acquire images from the SLO and OCT channels in rapid sequence while the LSO, AO, HS-WS, and RT are all running continuously. This was done in a unique configuration whereby the SLO timing board (that drives the scanners) can accept input from either the SLO RS or the OCT swept source. Thus the multiple scanning schemes available for both modes (OCT line and raster, SLO raster, montages, strip scans, etc.) use all the same hardware (scanners, real time processing board) and are set up from an extremely intuitive and flexible user interface.

We developed accompanying post-processing analysis routines for both SLO and OCT images including registration, montage and strip stitching, photoreceptor quantification, and segmentation (retinal layers and drusen) [33]. Some require limited user input (i.e., are semi-automated) while others operate in a fully automated manner (e.g., photoreceptor counting). With the multimodal image acquisition modes and these analysis tools, it is now possible to fully map retinal layers and critical structures across the macula [38].

In the next phase of the research, the system will be installed in an ophthalmology clinic, where it will be validated in studies designed to provide qualitative and quantitative information on the fine structural characteristics of several diseases, including glaucoma, diabetic retinopathy, age-related macular degeneration, and retinitis pigmentosa. We plan to examine vascular and other deeper structures by taking advantage of the enhanced penetration at 1 μm illumination.

5. Conclusion

Significant progress has been made toward the development of an innovative clinical multimodal AO retinal imaging platform. We designed, built, and tested a high performance device capable of collecting AO-enhanced SLO images to resolve cones within 0.5 deg of the fovea and AO enhanced OCT images with improved penetration for identification of all major retinal layers. We have also begun development of automated image quantification algorithms, which will streamline information extraction necessary for clinical deployment. The prototype system development will continue with future device refinement and extensive clinical testing.

Acknowledgements

This work was supported by NIH grant EY018986. We thank Stephen Burns, James Fujimoto, Joel Schuman, Gadi Wollstein, and Larry Kagemann for advice and assistance.